

PAPER

[View Article Online](#)
[View Journal](#) | [View Issue](#)
Cite this: *Nanoscale*, 2020, **12**, 17013

Selective electrochemical reduction of carbon dioxide to ethylene on a copper hydroxide nitrate nanostructure electrode†

Mang Wang, Qixing Zhang, Qixian Xie, Lili Wan, Ying Zhao, Xiaodan Zhang  and Jingshan Luo  *

Received 1st April 2020,
 Accepted 13th July 2020
 DOI: 10.1039/d0nr02591g
rsc.li/nanoscale

Electrochemical carbon dioxide reduction (CO_2 RR) is a promising technology to convert CO_2 into valuable carbon-based fuels and chemicals. Copper (Cu) is a unique catalyst for this reaction as it yields substantial hydrocarbon products, but still suffers from low selectivity in aqueous solution. Here, we present a nanostructure $\text{Cu}@\text{Cu}_2(\text{OH})_3\text{NO}_3$ electrode using a facile molten salt decomposition method (MSDM). Both XPS and XRD data indicate that $\text{Cu}_2(\text{OH})_3\text{NO}_3$ is converted into metallic Cu when employed in CO_2 electroreduction in KHCO_3 solution, leaving abundant defects on the dendritic rough surface. Benefiting from the defects and rough surface, this electrode exhibited a high selectivity for C_2H_4 production with a faradaic efficiency (FE) of 31.80% and a high stability for 20 h.

Introduction

The gigantic amount of CO_2 emission is responsible for global warming and climate change, which makes it urgent to reduce the concentration of CO_2 in the atmosphere.^{1,2} The electrochemical CO_2 reduction reaction driven by solar or wind electricity is a promising approach to close the anthropogenic carbon cycle.^{3,4} However, it remains challenging due to the low efficiency and poor product selectivity of the catalysts.⁵

Cu is the only single metal electrocatalyst that can catalyze electrochemical CO_2 reduction into value-added hydrocarbons, such as methane, ethylene, ethane, *etc.*^{6,7} Among these hydrocarbon products, ethylene (C_2H_4) attracted more attention due to its higher market value compared to others.^{8,9} However, the FE of C_2H_4 on metallic Cu is still low, due to the competitive production of H_2 and other carbonaceous species. Thus, many strategies have been tried to improve the FE of ethylene on the Cu electrode, such as morphology control,¹⁰ oxide-derived copper,^{11–13} copper-based bimetal catalysts,^{2,4} heteroatom doping,^{14,15} facet control,^{9,12,16} and molecular modification.¹⁷ Among all strategies, defect engineering, including grain boundaries,¹¹ steps,¹⁸ and vacancies,¹⁹ holds a unique posi-

tion, because the abundant low-coordinated atoms near the defect sites could chemisorb and stabilize the critical reaction intermediates (CO and others) for subsequent reduction into C_{2+} products.^{20,21}

For instance, a Cu^{2+} ion cycling method was used to deposit Cu nanocubes preferentially exposing the Cu (100) and stepped (211) facets on Cu foil which are favorable for CO dimerization. As a result, the electrode showed a highest FE of 32% for C_2H_4 and 60.5% for C_{2+} products in KHCO_3 solution.¹¹ In addition to the preferentially exposed facets, there should be abundant grain boundaries formed during the Cu nanocube formation, which also plays a significant role in CO_2 electroreduction according to the previous work of the Kanan group.^{12,22}

Defects can also be introduced into the catalyst by rational design. For example, steps and edges with low-coordinated Cu atoms were introduced into a nanoporous copper film by the additive-controlled electrodeposition method.¹⁸ Benefiting from the steps and edges, the electrode showed a high CO_2 reduction selectivity with a FE of 40% for C_2H_4 and a FE of 20% for $\text{C}_2\text{H}_5\text{OH}$ production. In addition, partially reduced copper oxide nanodendrites with rich surface oxygen vacancies ($\text{CuO}_x\text{-Vo}$) were developed. Theoretical calculations revealed that the oxygen vacancies could bind the intermediates of $^*\text{CO}$ and $^*\text{COH}$ strongly but bind $^*\text{CH}_2$ weakly. Thus, they significantly enhance the formation rate of ethylene and lead to high selectivity for ethylene production with a FE of 63%.²⁰

Moreover, a catalyst with abundant steps can also be prepared by using the intermediate as a selective capping agent.²³ According to this strategy, a self-selective catalyst, Cu

Institute of Photoelectronic Thin Film Devices and Technology, Solar Energy Research Center, Key Laboratory of Photoelectronic Thin Film Devices and Technology of Tianjin, Ministry of Education Engineering Research Center of Thin Film Photoelectronic Technology, Nankai University, Tianjin 300350, China.
 E-mail: jingshan.luo@nankai.edu.cn

†Electronic supplementary information (ESI) available. See DOI: 10.1039/d0nr02591g

(SELF-CAT-Cu), with a large portion of Cu steps on the surface exhibited a high selectivity for C_{2+} products with a FE of 42.2%. In comparison, the normal Cu without steps only obtained a FE of 20.9%.

Inspired by the above reports, we prepared a Cu mesh-supported copper hydroxide nitrate ($Cu@Cu_2(OH)_3NO_3$) electrode *via* a simple molten salt decomposition method. The $Cu_2(OH)_3NO_3$ layer was converted into dendritic metallic Cu through an electro-redeposition process during the CO_2 reduction reaction, which also induced grain boundaries (GB) and abundant defects with low-coordinated Cu atoms on the nano-dendritic surface. We hypothesize that the GB and defect sites would chemisorb and stabilize the reaction intermediates, and together with the rough surface could result in a significant rise in the local pH, which would suppress methane formation and finally improve the selectivity for C_2H_4 production.

Experimental section

Preparation of the $Cu@Cu_2(OH)_3NO_3$ electrode

The Cu mesh-supported $Cu_2(OH)_3NO_3$ electrode ($Cu@Cu_2(OH)_3NO_3$) was prepared by a molten salt decomposition method according to the previous literature with slight modifications.²⁴ Typically, a Cu mesh was washed with ethanol, dilute HCl and water in sequence with sonication for 10 minutes respectively, and dried under a N_2 flow. Then, 5 g of $Cu(NO_3)_2 \cdot H_2O$ in a clean beaker was placed in an oil bath at 140 °C for 15 minutes. The pretreated Cu mesh was added when $Cu(NO_3)_2 \cdot H_2O$ melted, and then kept for 5 minutes. The beaker was taken out from the oil bath and cooled to room temperature naturally. After rinsing with copious DI water and

drying in a vacuum oven, the light-blue electrode was prepared.

Characterization of the $Cu@Cu_2(OH)_3NO_3$ electrode

X-ray diffraction (XRD) was employed to analyze the chemical composition of the $Cu@Cu_2(OH)_3NO_3$ electrode (Fig. 1a). Three strong peaks marked as clubs belong to the Cu mesh.²⁵ The typical peaks emerging at (12.74), (21.6), (25.76), (31.98), (33.64), (36.42), (58.32) and (61.06) can be indexed to the (001), (110), (002), (200), (120), (121), (231) and (033) planes of $Cu_2(OH)_3NO_3$, respectively (PDF# 75-1779),^{24,26} indicating the successful fabrication of the $Cu@Cu_2(OH)_3NO_3$ electrode.

The morphology of the $Cu@Cu_2(OH)_3NO_3$ electrode was investigated by scanning electron microscopy (SEM) and transmission electron microscopy (TEM). The SEM images (Fig. 1b and Fig. S1†) show that the Cu fiber was uniformly covered with the $Cu_2(OH)_3NO_3$ nanorod. The TEM image (Fig. 1c) further reveals a regular rod-like morphology with a width of about 50 nm. Elemental mapping analysis of the TEM (Fig. 1d–g) and SEM (Fig. S2b–e†) images shows that Cu, O, and N are homogeneously distributed in the nanorod. Energy-dispersive X-ray spectroscopy (EDS, Fig. S2f†) further proves that Cu, O, and N are the principal elemental components, and the atomic ratio of Cu : O : N = 3.05 : 8.83 : 1.59, close to the ratio in the molecular formula (2 : 6 : 1), further demonstrating the successful preparation of the $Cu@Cu_2(OH)_3NO_3$ electrode.

The elemental composition and chemical states of the pristine $Cu@Cu_2(OH)_3NO_3$ electrode were investigated by X-ray photoelectron spectroscopy (XPS, Fig. 2). The survey spectrum (Fig. 2a) clearly exhibits the element signals of Cu, O and N, which were consistent with the EDX results. The peaks at 935.35 and 955.21 eV are attributed to $Cu^{2+} 2p_{3/2}$ and $Cu^{2+} 2p_{1/2}$ in the $Cu_2(OH)_3NO_3$ layer, respectively (Fig. 2b). The O 1s

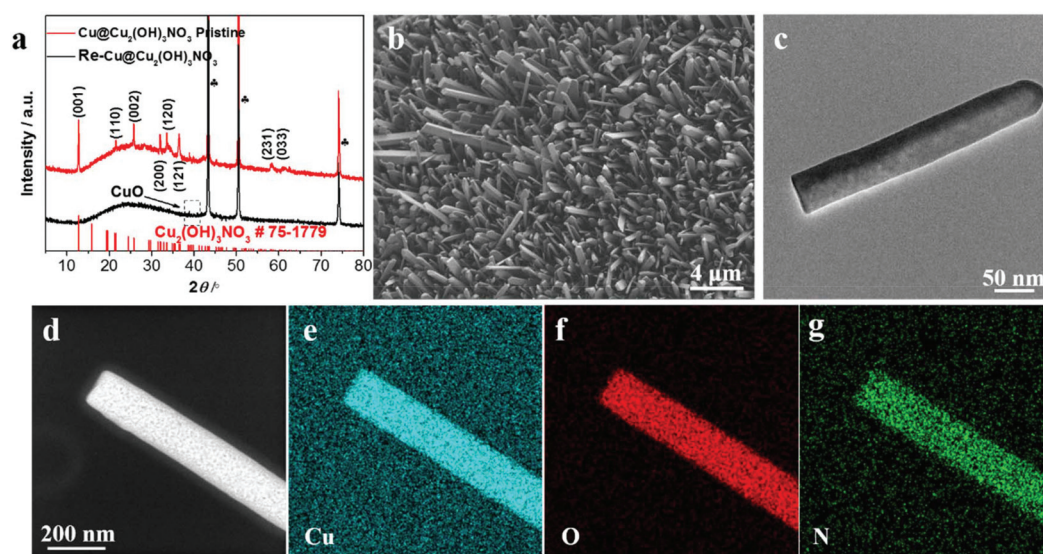


Fig. 1 (a) XRD patterns of the $Cu@Cu_2(OH)_3NO_3$ electrode before (red) and after (black) pre-reduction, (b) SEM and (c) TEM images of the pristine $Cu@Cu_2(OH)_3NO_3$ electrode, (d) HAADF-STEM image and the corresponding elemental mapping images of (e) Cu, (f) O, and (g) N.

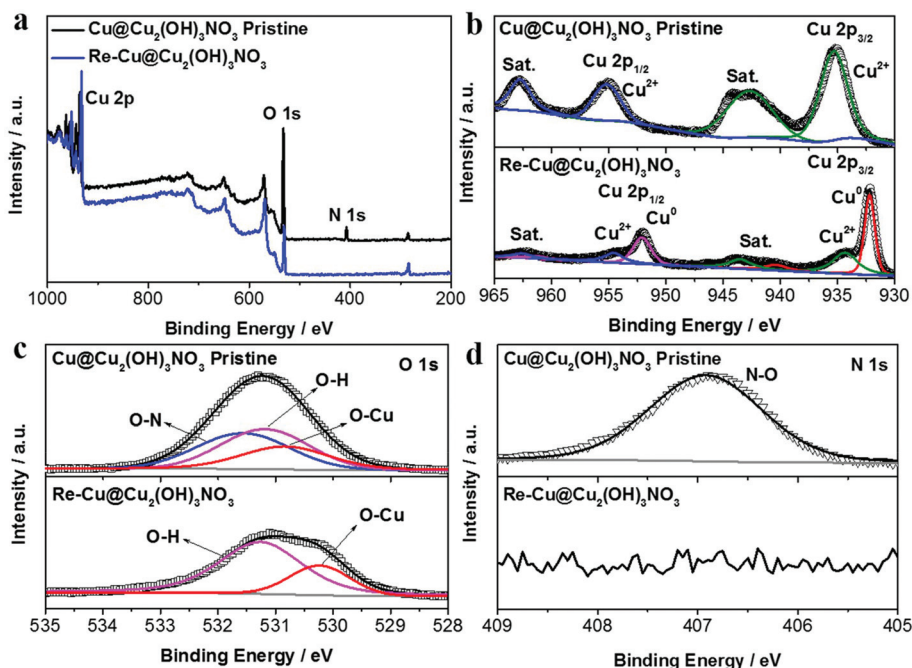


Fig. 2 (a) XPS survey spectra and high-resolution XPS spectra of (b) Cu 2p, (c) O 1s, and (d) N 1s of the $\text{Cu@Cu}_2(\text{OH})_3\text{NO}_3$ electrode before and after pre-reduction.

peak can be deconvoluted into three components: the O–N bond (532.56 eV), the O–H bond (adsorbed oxygen or hydroxide, 532.18 eV), and the O–Cu bond (lattice oxygen, 531.84 eV) (Fig. 2c). The symmetric N 1s peak at 406.91 eV can be assigned to NO_3^- (Fig. 2d).^{24,26} The XPS results together with the XRD data strongly indicate the successful preparation of the $\text{Cu@Cu}_2(\text{OH})_3\text{NO}_3$ electrode.

CO_2 electroreduction performance

The $\text{Cu@Cu}_2(\text{OH})_3\text{NO}_3$ electrode was pre-reduced before the electrochemical characterization, and the reduced electrode was labeled as the $\text{Re-Cu@Cu}_2(\text{OH})_3\text{NO}_3$ electrode hereafter. Both XRD (Fig. 1a) and XPS data (Fig. 2a–d) reveal that the $\text{Cu}_2(\text{OH})_3\text{NO}_3$ nanorod was reduced to metallic Cu,²⁷ but there were some signals of CuO on the surface of the $\text{Re-Cu@Cu}_2(\text{OH})_3\text{NO}_3$ electrode, which might be due to oxidation in air.²¹ TEM and SEM images show that the morphology of the nanorods changed to nanodendrites after pre-reduction (Fig. 3a, b and Fig. S3†), similar to the $\text{Cu}_2(\text{OH})_3\text{Cl}$ -derived ERD Cu (electro-redeposition copper), which undergoes dissolution and redeposition of copper from a sol-gel.²⁸ So we hypothesise that our electrode also underwent an electro-redeposition process during the pre-reduction, and NO_3^- would leach from the rods during this process. Elemental mapping analysis of the SEM image (Fig. 3c–e and Fig. S4b–e†) showed that Cu and O are homogeneously distributed on the surface of the $\text{Re-Cu@Cu}_2(\text{OH})_3\text{NO}_3$ electrode, which is consistent with the XRD and XPS data. A trace amount of the N signal might originate from the background or adsorbed contaminant. EDS revealed that the Cu:O:N ratio was 16.42:1:0,

further excluding the retention of NO_3^- in the electrode (Fig. S4f†).

Linear sweep voltammetry (LSV) was first conducted to evaluate the CO_2 RR performance on the $\text{Re-Cu@Cu}_2(\text{OH})_3\text{NO}_3$ electrode (Fig. 4a). Under Ar purge conditions, the current is mainly ascribed to the hydrogen evolution reaction, the major side reaction during the CO_2 reduction reaction. Under CO_2 bubbling conditions, an enhanced current density is observed, indicating that the CO_2 reduction reaction occurs readily on the $\text{Re-Cu@Cu}_2(\text{OH})_3\text{NO}_3$ electrode. A similar trend also appears in the Cu mesh electrode, which acts as a control sample (Fig. S5†).

It is well known that the selectivity of CO_2 RR is dependent on the applied potential.²⁹ Therefore, the chronoamperometry (CA) experiments were performed at different potentials to measure the FEs of different products. The total FE of all detectable products amounts to 87.64–95.48%, which indicates that the system was well calibrated (Fig. S6 and 7†). The product distribution trend exhibited by the bare Cu mesh electrode is consistent with previous studies^{29,30} (Fig. S6 and Table S1†), where CH_4 dominates the carbonaceous products with a highest FE of 49.68%. In contrast, the highest FE for C_2H_4 is only 15.77%. When CO_2 reduction is performed on the $\text{Re-Cu@Cu}_2(\text{OH})_3\text{NO}_3$ electrode (Fig. 4b, Fig. S7 and Table S2†), CH_4 production dramatically decreases with a FE less than 2%. This may result from the high local pH value on the surface of the electrode where the protonation of CO and methane formation were suppressed.¹³ As a result, the FE of C_2H_4 is improved to 31.80%. It is interesting to observe that the increase of the FE of C_2H_4 is accompanied by the decrease

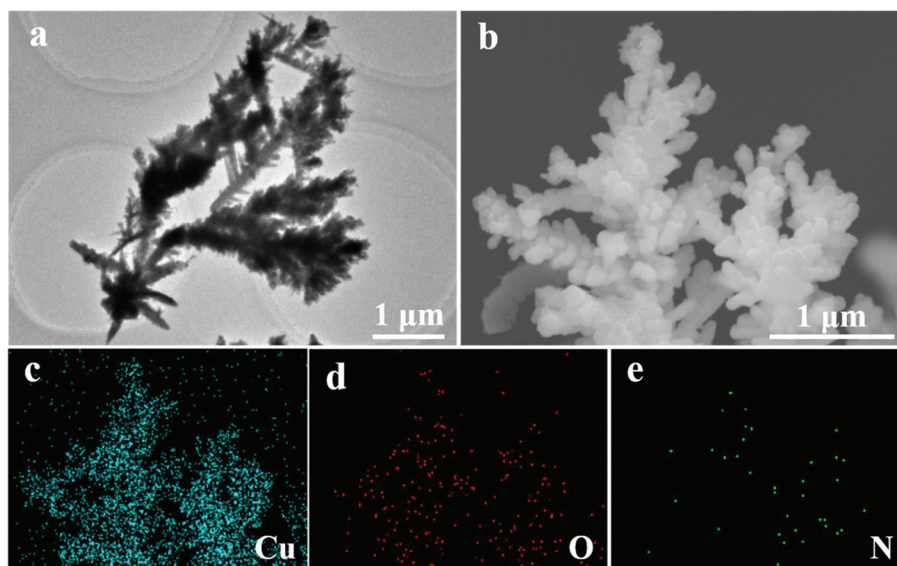


Fig. 3 (a) TEM and (b) SEM images and the corresponding elemental mapping images of (c) Cu, (d) O, and (e) N of the Re-Cu@Cu₂(OH)₃NO₃ electrode.

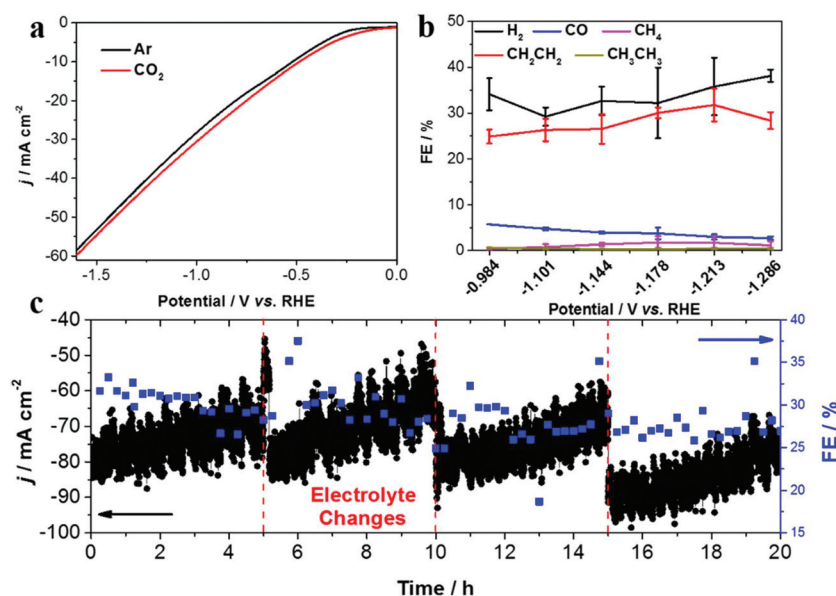


Fig. 4 (a) LSV curves of the Re-Cu@Cu₂(OH)₃NO₃ electrode in Ar (black) and CO₂ (red) saturated 0.1 M KHCO₃ solution, without stirring, scan rate: 20 mV s⁻¹, (b) the FE of the gaseous products as a function of applied potentials on the Re-Cu@Cu₂(OH)₃NO₃ electrode, and (c) long-term stability at -1.213 V (vs. RHE) of the Re-Cu@Cu₂(OH)₃NO₃ electrode.

of CO. In other words, C₂H₄ was produced primarily at the expense of CO evolution. This behavior is consistent with previous reports where CO is the intermediate in the formation of C₂₊ products.^{17,23,28} It should be noted that the FE of H₂ increased compared with the Cu mesh electrode, which may be the result of the enhanced adsorption of hydrogen (*H) on the surface of the electrode.³¹ Formate is the primary liquid product under all potentials with a highest FE of 18.20%.

To evaluate the stability of the Re-Cu@Cu₂(OH)₃NO₃ electrode, electrolysis at a fixed potential (-1.213 V vs. RHE) was carried out (Fig. 4c). The FE of C₂H₄ remained around 30% over 20 h with three time intervals. During each time interval, the current density decreased from 80 mA cm⁻² to 60 mA cm⁻² gradually. This phenomenon reemerges when fresh electrolyte was added, which indicates that it is due to the vaporization of the catholyte rather than the deactivation of the electrode.

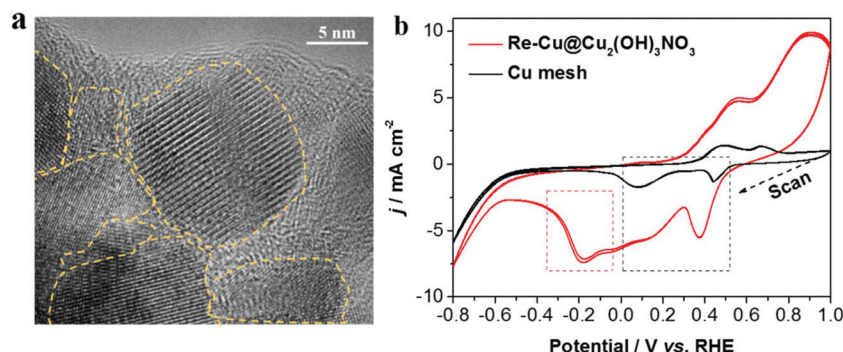


Fig. 5 (a) HRTEM image of the Re-Cu@Cu₂(OH)₃NO₃ nanodendrite and (b) cyclic voltammograms of the Re-Cu@Cu₂(OH)₃NO₃ and bare Cu mesh electrodes in 0.1 M KHCO₃ (saturated with Ar) for four segments respectively, without stirring, scan rate: 20 mV s⁻¹.

This result demonstrates that the Re-Cu@Cu₂(OH)₃NO₃ electrode possesses excellent stability.

Discussion

Compared with the bare Cu mesh electrode, the Re-Cu@Cu₂(OH)₃NO₃ electrode showed an almost complete suppression of CH₄ formation with an improved C₂H₄ formation. We attribute the enhanced selectivity of C₂H₄ to two main reasons: high local pH and defects.

On the one hand, Cu₂(OH)₃NO₃ was reduced to metallic Cu, leaving a dendritic rough surface after pre-reduction. These dense nanodendrites increase the surface roughness, leading to the mass diffusion limitations and further cause a high local pH value at the electrode and electrolyte interface. Because the CH₄ formation is pH dependent and the C₂H₄ formation is pH independent, finally the CH₄ formation is suppressed while the C₂H₄ formation is enhanced.¹³

On the other hand, during the pre-reduction process, there are abundant grain boundaries and defects with low-coordinated Cu atoms formed on the electrode. The defect sites on Cu-based electrocatalysts are important for reducing CO₂ to C₂₊ compounds, because they could adsorb the intermediate (CO) stronger, benefiting the subsequent deep reduction and the formation of C₂₊ products.^{20,21} Here, three methods were used to identify the defect sites. First, HRTEM (high-resolution TEM) images (Fig. 5a and Fig. S8†) clearly show abundant grain boundaries (one kind of defect) exposed on the surface of Cu₂(OH)₃NO₃-derived Cu. The second one is the voltammetry signatures as shown in the cyclic voltammograms of the Re-Cu@Cu₂(OH)₃NO₃ electrode and the bare Cu mesh electrode (Fig. 5b and Fig. S9†). Both electrodes exhibited two major reduction peaks in the potential range of 0–0.5 V (vs. RHE, marked in the black frame), which can be assigned to the reduction peaks of Cu²⁺/Cu⁺ and Cu⁺/Cu⁰ couples,³² respectively. Interestingly, a reduction peak at ~−0.18 V was identified on the Re-Cu@Cu₂(OH)₃NO₃ electrode only (marked in the red frame). This peak is assigned to the reduction of Cu defect sites according to the previous literature.^{33,34} The peak is detectable after 20 h of continuous electrolysis (marked in the red frame), also demonstrating that the defects are stable

during the long-term CO₂ reduction experiment (Fig. S10†). Third, it has been reported that the surface defects (vacancy) can be evaluated by the ratio between the XPS peaks of adsorbed oxygen (O_{ads}) and lattice oxygen (O_{latt}), and the higher ratio indicates a larger amount of surface oxygen vacancies.²⁰ Thus, we carefully calculated the ratios before and after the pre-reduction. The ratio of adsorbed oxygen (O_{ads}) to lattice oxygen (O_{latt}) after pre-reduction is 2.94, nearly twice the ratio before pre-reduction (1.59, Table S3†), though there is a huge amount of hydroxide (OH[−]) in the Cu₂(OH)₃NO₃ crystal. This indicates that the Re-Cu@Cu₂(OH)₃NO₃ electrode possesses a high density of defect sites on the surface.

Possible reaction pathway

Based on the previous literature,^{21,35} the possible reaction pathway of the enhanced selectivity to C₂H₄ on the Re-Cu@Cu₂(OH)₃NO₃ electrode is proposed, Fig. 6. The first step involves electron and proton transfer to form a *COOH intermediate, which is hydrogenated to give moderately adsorbed *CO on the defect-rich surface. Then *CO might proceed through three different paths to form the C₂H_xO₂ intermediate, which will be finally reduced to produce C₂H₄. Path I involves the C–C coupling between two *CO intermediates.

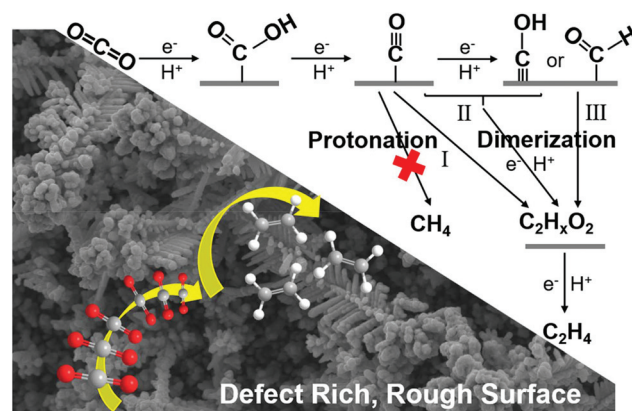


Fig. 6 Proposed pathway for the electroreduction of CO₂ to ethylene on the Re-Cu@Cu₂(OH)₃NO₃ electrode.

Path II involves the hydrogenation of *CO to $^*CHO/^*COH$, followed by C–C coupling between *CO and $^*CHO/^*COH$. Path III involves the C–C coupling between $^*CHO/^*COH$ and $^*CHO/^*COH$. Due to the high local pH caused by the rough dendritic surface, the protonation of CO into CH_4 is suppressed. Meanwhile, the defect-rich surface could chemisorb and stabilize the intermediates, finally resulting in an enhanced selectivity for C_2H_4 .

Conclusion

In summary, a facile molten salt decomposition method was employed to prepare the $Cu@Cu_2(OH)_3NO_3$ electrode for electrochemical CO_2 reduction. The $Cu_2(OH)_3NO_3$ nanocrystal on the surface of the electrode was converted into metallic Cu after pre-reduction, leaving abundant defects on the dendritic rough surface, which were identified by HRTEM, electrochemical method and XPS. Benefiting from the high density of defects and the high local pH, the $Re-Cu@Cu_2(OH)_3NO_3$ electrode exhibited a high selectivity for C_2H_4 production with a FE of 31.80% and a high stability for more than 20 h. This work opens up exciting new avenues to explore Cu-based electrodes for electrochemical carbon dioxide reduction.

Conflicts of interest

There are no conflicts to declare.

Acknowledgements

J. L. acknowledges the funding support from the Fundamental Research Funds for the Central Universities, Nankai University (63201178) and the Overseas Expertise Introduction Project for Discipline Innovation of Higher Education of China (Grant No. B16027).

References

- 1 L. Zhang, Z. Zhao and J. Gong, *Angew. Chem., Int. Ed.*, 2017, **56**, 11326–11417.
- 2 T. Hoang, S. Verma, S. Ma, T. Fister, J. Timoshenko, A. Frenkel, P. Kenis and A. A. Gewirth, *J. Am. Chem. Soc.*, 2018, **140**(17), 5791–5797.
- 3 M. Schreier, F. Héroguel, L. Steier, S. Ahmad, J. Luterbacher, M. Mayer, J. Luo and M. Grätzel, *Nat. Energy*, 2017, **2**, 17087–17096.
- 4 J. Gao, H. Zhang, X. Guo, J. Luo, S. Zakeeruddin, D. Ren and M. Grätzel, *J. Am. Chem. Soc.*, 2019, **141**(47), 18704–18714.
- 5 C. Dinh, T. Burdyny, M. Kibria, A. Seifitokaldani, C. Gabardo, F. Arquer, A. Kiani, J. Edwards, P. Luna, O. Bushuyev, C. Zou, R. Bermudez, Y. Pang, D. Sinton and E. Sargent, *Science*, 2018, **360**, 783–787.
- 6 S. Nitopi, E. Bertheussen, S. Scott, X. Liu, A. Engstfeld, S. Horch, B. Seger, I. Stephens, K. Chan, C. Hahn, J. Nørskov, T. Jaramillo and Ib Chorkendorff, *Chem. Rev.*, 2019, **119**, 7610–7672.
- 7 G. Britovsek, M. Bruce, V. Gibson, B. Kimberley, P. Maddox, S. Mastroianni, S. McTavish, C. Redshaw, G. Solan, S. Strömberg, A. White and D. Williams, *J. Am. Chem. Soc.*, 1999, **121**, 8728–8740.
- 8 Y. Zhang, V. Sethuraman, R. Michalsky and A. Peterson, *ACS Catal.*, 2014, **4**, 3742–3748.
- 9 Y. Gao, Q. Wu, X. Liang, Z. Wang, Z. Zheng, P. Wang, Y. Liu, Y. Dai, M. Whangbo and B. Huang, *Adv. Sci.*, 2020, 1902820–1902827.
- 10 M. Ma, K. Djanashvili and W. Smith, *Angew. Chem., Int. Ed.*, 2016, **55**, 6680–6684.
- 11 C. W. Li and M. W. Kanan, *J. Am. Chem. Soc.*, 2012, **134**, 7231–7234.
- 12 K. Jiang, R. Sandberg, A. Akey, X. Liu, D. Bell, J. Nørskov, K. Chan and H. Wang, *Nat. Catal.*, 2018, **1**, 111–119.
- 13 H. Mistry, A. Varela, C. Bonifacio, I. Zegkinoglou, I. Sinev, Y. Choi, K. Kisslinger, E. Stach, J. Yang, P. Strasser and B. Cuenya, *Nat. Commun.*, 2016, **7**, 12123–12130.
- 14 Z. Liang, T. Zhuang, A. Seifitokaldani, J. Li, C. Huang, C. Tan, Y. Li, P. Luna, C. Dinh, Y. Hu, Q. Xiao, P. Hsieh, Y. Wang, F. Li, R. Bermudez, Y. Zhou, P. Chen, Y. Pang, S. Lo, L. Chen, H. Tan, Z. Xu, S. Zhao, D. Sinton and E. Sargent, *Nat. Commun.*, 2018, **9**, 3828–3836.
- 15 D. Gao, I. Sinev, F. Scholten, R. Arán-Ais, N. Divins, K. Kvashnina, J. Timoshenko and B. Cuenya, *Angew. Chem., Int. Ed.*, 2019, **58**, 2–9.
- 16 Y. Hori, I. Takahashi, O. Koga and N. Hoshi, *J. Phys. Chem. B*, 2002, **106**, 15–17.
- 17 F. Li, A. Thevenon, A. Rosas-Hernández, Z. Wang, Y. Li, C. Gabardo, A. Ozden, C. Dinh, J. Li, Y. Wang, J. Edwards, Y. Xu, C. McCallum, L. Tao, Z. Liang, M. Luo, X. Wang, H. Li, C. O'Brien, C. Tan, D. Nam, R. Bermudez, T. Zhuang, Y. Li, Z. Han, R. Britt, D. Sinton, T. Agapie, J. Peters and E. Sargent, *Science*, 2020, **577**, 509–513.
- 18 T. Hoang, S. Ma, J. Gold, P. Kenis and A. Gewirth, *ACS Catal.*, 2017, **7**, 3313–3321.
- 19 Z. Geng, X. Kong, W. Chen, H. Su, Y. Liu, F. Cai, G. Wang and J. Zeng, *Angew. Chem., Int. Ed.*, 2018, **57**, 6054–6059.
- 20 Z. Gu, N. Yang, P. Han, M. Kuang, B. Mei, Z. Jiang, J. Zhong, L. Li and G. Zheng, *Small Methods*, 2018, 1800449–1800457.
- 21 D. Ren, Y. Deng, A. Handoko, C. Chen, S. Malkhandi and B. Yeo, *ACS Catal.*, 2015, **5**, 2814–2821.
- 22 Y. Chen, C. W. Li and M. W. Kanan, *J. Am. Chem. Soc.*, 2012, **134**, 19969–19972.
- 23 H. Wang, Z. Liang, M. Tang, G. Chen, Y. Li, W. Chen, D. Lin, Z. Zhang, G. Zhou, J. Li, Z. Lu, K. Chan, T. Tan and Y. Cui, *Joule*, 2019, **3**, 1–10.
- 24 Y. Ma, J. Chu, Z. Li, D. Rakov, X. Han, Y. Du, B. Song and P. Xu, *Small*, 2018, **14**, 1803783–1803790.

- 25 M. Ma, K. Djanashvili and W. A. Smith, *Angew. Chem., Int. Ed.*, 2016, **55**, 6680–6684.
- 26 L. Di, D. Duan, Z. Zhan and X. Zhang, *Adv. Mater.*, 2016, 1600760–1600765.
- 27 D. Ren, J. Gao, L. Pan, Z. Wang, J. Luo, S. Zakeeruddin, A. Hagfeldt and M. Grätzel, *Angew. Chem.*, 2019, **131**, 15178–15182.
- 28 P. Luna, R. Q. Bermudez, C. T. Dinh, M. B. Ross, O. S. Bushuyev, P. Todorović, T. Regier, S. O. Kelley, P. Yang and E. H. Sargent, *Nat. Catal.*, 2018, **1**, 103–110.
- 29 D. Ren, J. Fong and B. S. Yeo, *Nat. Commun.*, 2018, **9**, 925–933.
- 30 K. Manthiram, B. J. Beberwyck and A. P. Alivisatos, *J. Am. Chem. Soc.*, 2014, **136**, 13319–13325.
- 31 M. Luo, Z. Wang, Y. C. Li, J. Li, F. Li, Y. Lum, D. Nam, B. Chen, J. Wicks, A. Xu, T. Zhuang, W. Leow, X. Wang, C. Dinh, Y. Wang, Y. Wang, D. Sinton and E. Sargent, *Nat. Commun.*, 2019, **10**, 5814–5821.
- 32 W. Tang, A. Peterson, A. Varela, Z. Jovanov, L. Bech, W. Durand, S. Dahl, J. Nørskov and Ib Chorkendorff, *Phys. Chem. Chem. Phys.*, 2012, **14**, 76–81.
- 33 D. Ren, N. Wong, A. Handoko, Y. Huang and B. S. Yeo, *J. Phys. Chem. Lett.*, 2016, **7**, 20–24.
- 34 H. Jeon, S. Kunze, F. Scholten and B. Cuenya, *ACS Catal.*, 2018, **8**, 531–535.
- 35 W. Ma, S. Xie, T. Liu, Q. Liu, Q. Fan, J. Ye, F. Sun, Z. Jiang, Q. Zhang, J. Cheng and Y. Wang, *Nat. Catal.*, 2020, **3**, 478–487.